Applied Physics Letters

RESEARCH ARTICLE | JUNE 03 2024

Antenna-enhanced high-resistance photovoltaic infrared detectors based on quantum ratchet architecture

Hideki T. Miyazaki ; Takaaki Mano ; Takeshi Noda ; Takeshi Kasaya ; Yusuf B. Habibullah

Appl. Phys. Lett. 124, 231103 (2024)
https://doi.org/10.1063/5.0208399

Applied Physics Letters ARTICLE pubs.aip.org/aip/apl

Antenna-enhanced high-resistance photovoltaic infrared detectors based on quantum ratchet architecture

Cite as: Appl. Phys. Lett. **124**, 231103 (2024); doi: 10.1063/5.0208399
Submitted: 14 March 2024 · Accepted: 23 May 2024 ·
Published Online: 3 June 2024

Hideki T. Miyazaki,[a] Takaaki Mano, Takeshi Noda, Takeshi Kasaya, and Yusuf B. Habibullah[b]

AFFILIATIONS

National Institute for Materials Science, Tsukuba 305-0047, Japan

[a]**Author to whom correspondence should be addressed:** miyazaki.hideki@nims.go.jp
[b]**Present address:** Rakuten Mobile, Inc., Tokyo 158-0094, Japan.

ABSTRACT

We demonstrate a quantum ratchet detector, which is a high-resistance photovoltaic mid-infrared detector based on an engineered spatial arrangement of subbands. In photovoltaic quantum-well photodetectors, in which unidirectional photocurrent is generated by asymmetric quantum-well structures, maximization of device resistance by suppressing undesired electron transports is crucial for minimizing noise. A semi-quantitative guideline suggests the significance of spatial separation between wavefunctions for reducing the conductance from the ground state. Here, we employ a step quantum well made of a shallow floor and a deep well. Photoexcited electrons are quickly transferred to a separated location from the ground state through fast resonant tunneling and phonon scattering, and then they are allowed to flow in only one direction. This architecture is made possible by the use of a GaAs/AlGaAs material system, and it achieves a resistance as high as $6.0 \times 10^4\,\Omega\mathrm{cm}^2$ with a single-period structure. Combined with optical patch antennas for responsivity enhancement, we demonstrate a maximum background-limited specific detectivity of $6.8 \times 10^{10}\,\mathrm{cmHz}^{1/2}/\mathrm{W}$ at 6.4 μm, 77 K for normal incidence, and a background-limited-infrared-photodetector temperature of 98 K.

Manipulation of intersubband transitions by engineered quantum-well (QW) structures is a key technology for mid-infrared region applications. Quantum cascade lasers have become dominant mid-infrared light sources.[1] In quantum-well infrared photodetectors (QWIPs), the necessity of an incident electric field vertical to the QWs has long been a problem.[2,3] However, recent progress in nanophotonics, particularly plasmonic antennas, has essentially solved the coupling issue with normally incident radiation.[4–9]

The majority of QWIPs have belonged to the photoconductive type. Nevertheless, the dark current due to bias voltage induces significant generation–recombination noise and limits the device operation to cryogenic temperatures. For imaging devices or uncooled detectors, photovoltaic (PV) QWIPs are advantageous because they do not require biasing and thus exhibit no dark current. PV-QWIPs based on asymmetric QW structures have been demonstrated since the early days of QWIP research.[10–12] The most promising scheme in this regard would be quantum cascade detectors (QCDs).[13–16] Performance enhancement of QCDs by incorporating micro/nanophotonics has also been attempted.[17–22]

In QCDs, the electrons are transported by tunneling and longitudinal optical (LO) phonon scattering through stairs of subbands. The difficulty in QCD design lies in the trade-off between responsivity and resistance.[15,16] For suppressing dominant Johnson noise, it is necessary to raise the resistance (R_0) area (A) product. Since the birth of QCDs, there have been various trials for improving R_0A, by methods such as thickening the barriers,[15,23] changing materials,[15,24,25] diagonal transition,[26] and using coupled QWs.[21] However, these efforts have remained within the framework of binary energy profiles.

In this Letter, we present a high-resistance PV-QWIP architecture, which we call a quantum ratchet detector (QRD), where the R_0A is raised by suppressing the overlap of wavefunctions using a step QW[27] to trap electrons at a distant location. With the aid of responsivity enhancement by optical antennas,[28–30] a single-period detector demonstrated a maximum background-limited specific detectivity of $6.8 \times 10^{10}\,\mathrm{cmHz}^{1/2}/\mathrm{W}$ at 6.4 μm, 77 K as well as a background-limited-infrared-photodetector (BLIP) temperature of 98 K. This performance is achieved through a high resistance of $6.0 \times 10^4\,\Omega\mathrm{cm}^2$, 29 times greater than conventional QCDs with a similar design.

The essential property of infrared detectors is expressed by its specific detectivity,[2,3,15,16] which is essentially the signal-to-noise ratio:

$$D^* = \frac{R_{esp}\sqrt{A}}{i_{nsd}}, \tag{1}$$

where R_{esp} is the responsivity and i_{nsd} is the current noise spectral density. Here, R_{esp} is given by

$$R_{esp} = \frac{e\lambda}{hc} \times \frac{\eta_{abs} p_e}{N_w}, \tag{2}$$

where e is the electron charge, λ the wavelength, h the Planck constant, c the speed of light, η_{abs} the absorption efficiency, p_e the escape probability, N_w the number of periods of the unit structure, and $\eta_{abs}p_e/N_w$ the external quantum efficiency (EQE).

Dark state and background state are key concepts in infrared detectors. In the dark state, the detector is covered with a cold shield and no radiation is incident. In the background state, the detector is exposed to radiation from a 300 K environment. The parameters corresponding to these two states are indicated by subscripts DK and BG, respectively.

Except for a special cryogenic region, the characteristics of a detector are expressed using dark-state properties, even in the background state. Therefore, we must first consider the dark-state properties. Here, $i_{nsd,DK}$ of a PV-QWIP is dominated by Johnson noise:[15,16]

$$i_{nsd,DK} = \sqrt{\frac{4k_B T}{R_0}}, \tag{3a}$$

where k_B is the Boltzmann constant and T is the temperature of the detector. Accordingly,

$$D^*_{DK} = R_{esp}\sqrt{\frac{R_0 A}{4k_B T}} \propto \eta_{abs} \times p_e \times \sqrt{R_0 A} \times \frac{1}{N_W}; \tag{3b}$$

raising η_{abs}, p_e, and R_0A and decreasing N_w is crucial for improving the D^*_{DK} of PV-QWIPs.

As T decreases, D^*_{DK} exponentially increases, and the detector finally enters the BLIP region, where the shot noise by detected background radiation from a 300 K environment is dominant.[15,16] Here, i_{nsd} and D^* for this region are given by

$$i_{nsd,BG} = \sqrt{\frac{2eAR_{esp,p}P_{BG,p}\Delta\lambda}{N_w}}, \tag{4a}$$

and

$$D^*_{BG} = \sqrt{\frac{\lambda_p \eta_{abs,p} p_e}{2hcP_{BG,p}\Delta\lambda}} \propto \sqrt{\eta_{abs,p} \times p_e}, \tag{4b}$$

where $R_{esp,p}$ is the peak responsivity, $P_{BG,p}$ the background Planck radiation intensity at the peak wavelength λ_p, $\Delta\lambda$ the effective bandwidth, and $\eta_{abs,p}$ the absorption efficiency at λ_p. See supplementary material S1 for details. In the BLIP region, D^* is solely determined by the responsivity ($\eta_{abs,p}$ and p_e), and R_0A no longer appears. However, a detector with a higher R_0A exhibits a higher D^*_{DK} and reaches the BLIP region at a higher temperature (BLIP temperature, T_{BLIP}). T_{BLIP} is a fundamental index of a photodetector that specifies its operation temperature; cooling a detector below T_{BLIP} will not lead to a D^* above D^*_{BG}, so long as it is used in a 300 K environment. Consequently, the higher the R_0A, the higher the T_{BLIP}, and the lower the burden of cooling the detector in practical use. T_{BLIP} values for conventional PV-QWIPs at similar wavelengths have been 70–83 K.[18,21]

Let us start with a discussion on the fundamental strategy for engineering R_0A. In a PV-QWIP (Fig. 1, inset), the electrons supplied from the left side are photoexcited at the active QW and then transferred to the right side through a series of subbands. The resistance can be expressed as the sum of the transition rates from the ground state of the active well S_1 to the other states:[31]

$$R_0 A = \frac{k_B T}{e^2 \sum_j G_{1j}}, \tag{5}$$

where G_{ij} is the global transition rate between states i (S_i) and j (S_j) for emission and absorption of LO phonons. Here, G_{ij} is essentially given by two factors: the overlap of wavefunctions of the two states (form factor)[32] and the Fermi–Dirac occupation factor, which express the effects of spatial and energetic distances between the states, respectively. G_{ij} can be viewed as the conductance between states due to its inverse relationship with resistance. The resistance of a PV-QWIP is dominated by the transport between S_1 and a few limited states S_j's with high conductance.

Figure 1 quantitatively displays the significance of the spatial and energetic distances between S_1 and S_j on R_0A for a model PV-QWIP (see supplementary material S2). The colors indicate the G_{1j} between

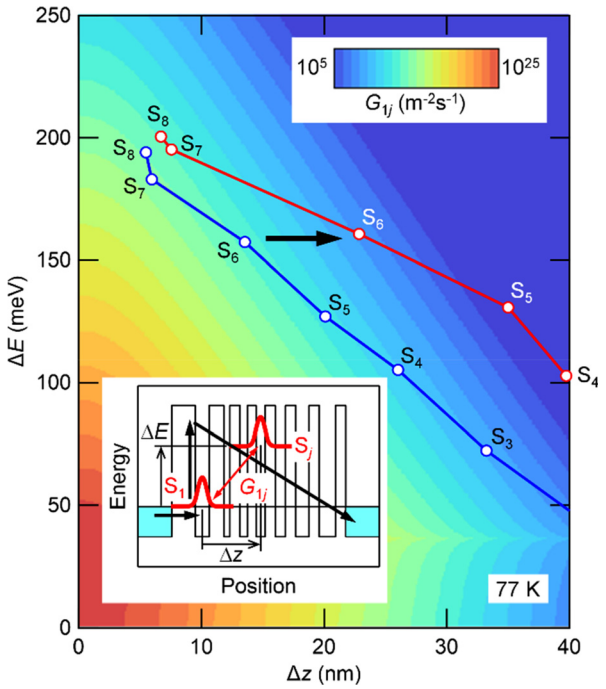

FIG. 1. Relationship of state-to-state conductance G_{1j} with spatial and energetic distances at 77 K assuming a 5-nm-wide QW. Each color step denotes one order difference. Inset: schematic of a generalized PV-QWIP. States 1 and j are separated by (Δz, ΔE). Superimposed curves represent actual (Δz, ΔE) positions in this paper (red: QRD and blue: QCD).

the ground state S_1 at the origin and a state S_j with an identical wavefunction shape virtually placed at $(\Delta z, \Delta E)$. As S_j moves away spatially (rightward) or energetically (upward), the conductance of the path exponentially decays. The horizontal singular peak at $\Delta E = \hbar\omega_{LO} = 36$ meV indicates the LO phonon scattering of GaAs.

For the energy ΔE of each state, the design freedom is limited, since this is determined by the target wavelength and energy step close to $\hbar\omega_{LO}$. However, we have sufficient freedom in the spatial location of the wavefunctions Δz, which should be maximized so long as faster forward transition than backward is achieved. Quantitatively, G_{1j} decreases by one order of magnitude for a spatial distance of $\Delta z_0 = 2.1$ nm and an energetic distance of $\Delta E_0 = 14.5$ meV. Considering the slope $\Delta z_0/\Delta E_0$, a spatial distance sufficiently exceeding $\Delta z \sim 5.2$ nm for a typical energy step of $\Delta E \sim \hbar\omega_{LO}$ is necessary for a significant reduction in the conductance. A structure keeping the wavefunction as far away as possible, preferably about 10 nm, would be necessary.

A band diagram of the proposed QRD made from GaAs/$Al_xGa_{1-x}As$ is shown in Fig. 2(a). The thickness of each layer (in nm) of the device region is as follows: **9.05**/5.09/**5.65**/11.31(0.32)/5.65 (0.25)/**5.65**/1.70/**3.96**/1.98/**3.96**/2.54/**3.96**/3.11/**3.96**, where AlGaAs barriers with $x = 0.40$ are shown in bold, the doped layer (Si, 1×10^{18} cm^{-3}) is underlined, and () denotes the x value of $Al_xGa_{1-x}As$ for some well regions.

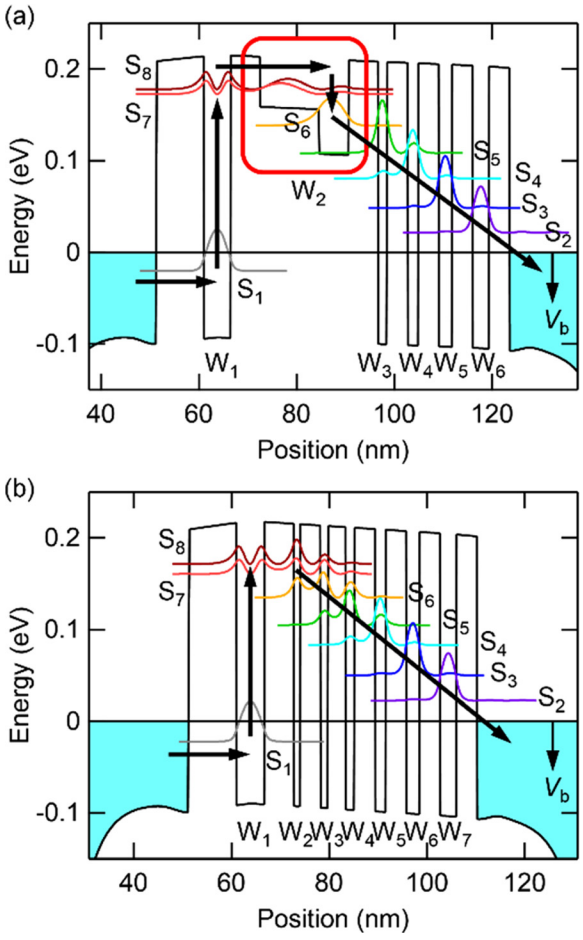

FIG. 2. Conduction band diagrams with squared wavefunction profiles for (a) the proposed QRD and (b) reference QCD. Black arrows indicate electron flow. Red frame in (a) shows the step QW.

Because R_{esp} is inversely proportional to N_w, $N_w = 1$ gives the highest R_{esp}.[7,9,22] In addition, for a single-period structure, the influence of the energy profile at individual parts can be straightforwardly observed and compared. Therefore, we employ $N_w = 1$. Both sides of the device region in Fig. 2 are Ohmically connected to electrodes through highly doped contact layers. The structure was designed aiming at a responsivity peak at $\lambda = 6.3$ μm.

For rapid transport of electrons from the active well W_1 to a distant location, we employed a step QW made of a shallow floor and a deep well as the second well, W_2 (Ref. 27) [represented by a red frame in Fig. 2(a)]. This structure is made possible by the use of a GaAs/AlGaAs material system, which permits an arbitrary conduction band offset by composition x. S_7 and S_8 are formed by tunnel coupling between the second states of W_1 and W_2, and the fundamental state S_6 of W_2 is located at $\sim\hbar\omega_{LO}$ below those levels. Electrons excited from S_1 to S_7 or S_8 by infrared absorption relax to S_6 at a rate of $\Gamma_{for} = 8.7 \times 10^{11}$ s^{-1} by LO phonon scattering (see supplementary material S3). This process is faster than the backward transition ($\Gamma_{back} = 3.9 \times 10^{11}$ s^{-1}) downward (to S_1) or leftward (to the left contact). Thus, the electrons preferentially flow in the right direction with a probability of $p_e = \Gamma_{for}/(\Gamma_{back} + \Gamma_{for}) = 0.69$.

The structure from W_3 was designed so that each subband descends by $\sim\hbar\omega_{LO}$ based on an earlier work.[23] The barriers here are slightly thicker than in the original study but are unified to the same thickness for easy interpretation of the results.

In this study, a conventional QCD with similar design parameters shown below is also discussed for a straightforward comparison [Fig. 2(b)]: **9.05**/5.37/**5.65**/1.13/**3.96**/1.41/**3.39**/1.70/**3.96**/1.98/**3.96**/2.54/**3.96**/3.11/**3.96**.

The conduction band forms a binary profile made of only two levels. The extraction region from W_4 is identical to that from W_3 in Fig. 2(a). Electrons excited from S_1 to S_7 or S_8 relax to S_6, which is $\sim\hbar\omega_{LO}$ below S_7/S_8, at a rate of $\Gamma_{for} = 1.22 \times 10^{12}$ s^{-1}, faster than the backward rate of $\Gamma_{back} = 4.7 \times 10^{11}$ s^{-1}; $p_e = 0.72$ is expected.

The locations of the gravity centers of the squared wavefunctions with respect to the ground state of the structures in Fig. 2 are plotted in Fig. 1. Note that the G_{1j} values for $j = 8$ and 7 are overestimated by 1–2 orders of magnitude in Fig. 1, since the actual wavefunctions for S_8 and S_7 have a very different form than the assumed shape. In the reference QCD, the G_{1j} values for $j = 6$ and 5 exhibit a substantial contribution to $\sum_j G_{1j}$. Therefore, these states short-circuit the electron flow to the ground state S_1 and limit R_0A to a low level. A more quantitative discussion is provided in supplementary material S2.

In contrast, in the proposed QRD, the location of S_6 is more distant by 9 nm than the reference QCD by the employment of the step QW, which suppresses the conductance by several orders of magnitude. Once the electrons are moved to such a far location, the backward transition from S_6 to the ground state S_1 then becomes negligible; S_6 functions as a ratchet to restrict the flow of electrons to one direction. Having no short-circuit path, QRDs can achieve drastically enhanced R_0A.

We fabricated both structures in Fig. 2 and compared their properties. The QWIP layer grown by molecular beam epitaxy on a GaAs

substrate was transferred to a Au substrate by wafer bonding and removal of the original substrate. The transferred QWIP layer includes the device region and contact layers consisting of a 20-nm-thick n-GaAs layer (Si, $2 \times 10^{18}\,\mathrm{cm}^{-3}$) and a 28-nm-thick heavily doped layer (Si, $5 \times 10^{18}\,\mathrm{cm}^{-3}$, and seven periodic δ-doped layers of $3 \times 10^{12}\,\mathrm{cm}^{-2}$) for nonalloyed Ohmic contact with the electrodes.[33] The actual QW structures suffered from fabrication errors, which are taken into consideration in the band diagrams in Fig. 2.

On a 160-μm-square QWIP layer, square Au patch antennas (side length: L) were periodically arranged (period: P) by electron beam drawing and liftoff in a 100-μm-square detector area. The fabricated antenna-enhanced QRD is shown in Fig. 3(a). On the Au patch side, the current laterally flows through the contact layer and reaches the surrounding electrode.[34] The QW structure in Fig. 2 rotated to the left by 90° is sandwiched between the Au patch and Au substrate. The electrode potential of the extractor side with respect to the W_1 side is defined as the bias voltage V_b. The Au patches were optimized to maximize the responsivity: $(L, P) = (0.87, 2.00)$ for QRD and (0.88, 1.90) for reference QCD in micrometers.

Electric field distribution of the QRD at the responsivity peak obtained by finite element analysis is displayed in Fig. 3(b). At the active QW (white dotted line), vertical electric field intensity is magnified 178 times at maximum.

The fabricated devices were installed in a cryostat with ZnSe windows, and their responsivity spectra were measured with a Fourier transform infrared spectrometer by feeding the amplified current signal to the external port. When required, lock-in measurement with a step-scan mode was used. The spectral responsivity was quantified based on a calibrated HgCdTe detector.

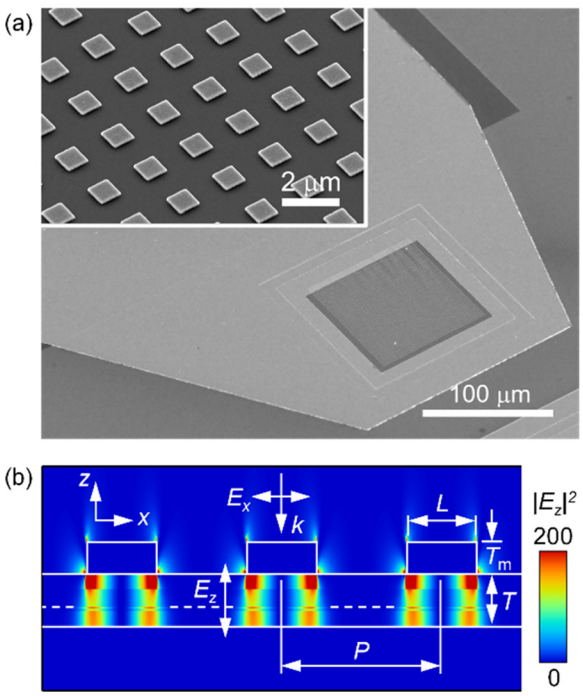

FIG. 3. (a) Scanning electron micrograph of a fabricated antenna-enhanced QRD. Inset: magnification of arrayed patch antennas. (b) Distribution of $|E_z|^2$ (E_z: vertical electric field) normalized by incident field for QRD at responsivity peak. Incident light: x-polarized, $\lambda = 6.4\,\mu$m, vertical incidence. Structure: $T = 164$ nm, $P = 2.00\,\mu$m, $L = 0.87\,\mu$m, and $T_m = 100$ nm.

The current–voltage relationship was measured with a source meter. The i_{nsd} was measured with a fast Fourier transform analyzer connected to a current amplifier in two environments: dark state and background state. The cryostat is equipped with a rotatable cold shield at 29 K with a blackbody coating. For the dark state, the detector was covered with the cold shield, while for the background state it was exposed to a 300 K environment with a field of view of 162°. See supplementary material S4 for details on fabrication, calculation, and characterization.

Figure 4(a) shows the current–voltage relationship for dark and background states. At zero bias, a photovoltaic signal higher than the dark current by several orders of magnitude is observed by background illumination. The dark current of the QRD is much lower than that of the QCD.

Figure 4(b) shows the responsivity spectra at 77 K. The value of $R_{esp,p}$ at zero bias for QRD was 0.207 A/W (EQE = 0.040, $\lambda = 6.40\,\mu$m), which was 36% of $R_{esp,p} = 0.570$ A/W for the reference QCD (0.106, 6.67 μm). However, by increasing the value of V_b, R_{esp} increased, and eventually both detectors exhibited similar maximum $R_{esp,p}$ values (QRD: $R_{esp,p} = 0.949$ A/W, EQE = 0.183; QCD: 0.931 A/W, 0.174). As shown in Fig. 4(c), two or three peaks emerge in $R_{esp,p}$ as V_b increases.

Compared with QCDs, in QRDs, more precise band alignment seems to be required for electron transport at zero bias. In addition, despite the design efforts aiming at an identical peak wavelength, the observed responsivity peak positions of the fabricated QRD and QCD showed a discrepancy. We attribute the incompleteness to inappropriate material parameters, particularly the conduction band offset, in the QW design. We also observed a change in the properties due to wafer bonding. Further refinement of the QW design and fabrication process is necessary.

Because η_{abs} is determined by the doping to the active QW, it should be identical in both detectors. Therefore, the maximum EQE of ~0.18 for the peak bias would represent η_{abs}. In this situation, the electrons are forcibly extracted to the right side; thus, $p_e \sim 1$ could be assumed (see supplementary material S5).

We can evaluate p_e at zero bias from the ratio of $R_{esp,p}$ at zero bias to that at peak bias from Eq. (2), since η_{abs} is almost the same at peak bias and zero bias, and p_e at peak bias is almost 1. At zero bias, $p_e = 0.61$ is estimated for the reference QCD, fairly consistent with the predicted value. In contrast, $p_e = 0.22$ for the QRD. With future optimization, improvement by a factor of ~3 is expected.

Figure 4(b) also presents the maximum R_{esp} based on calculation, which is 40% higher than the observed maximum R_{esp}. This could be due to excess absorption loss in the fabricated detectors or an overestimation of the imaginary part of the dielectric constant of W_1 used in the calculation. However, this discrepancy would be within a reasonable range.

Figure 5(a) shows the temperature dependence of i_{nsd} for both the dark and background states. Lower noise for the QRD is confirmed. The inset shows the Arrhenius plot displaying the temperature dependence of R_0A for dark current. At 77 K, QRD and QCD exhibit $R_0A = 6.0 \times 10^4$ and $2.1 \times 10^3\,\Omega\mathrm{cm}^2$, respectively. Resistance improvement by 29 times was achieved using the ratchet architecture.

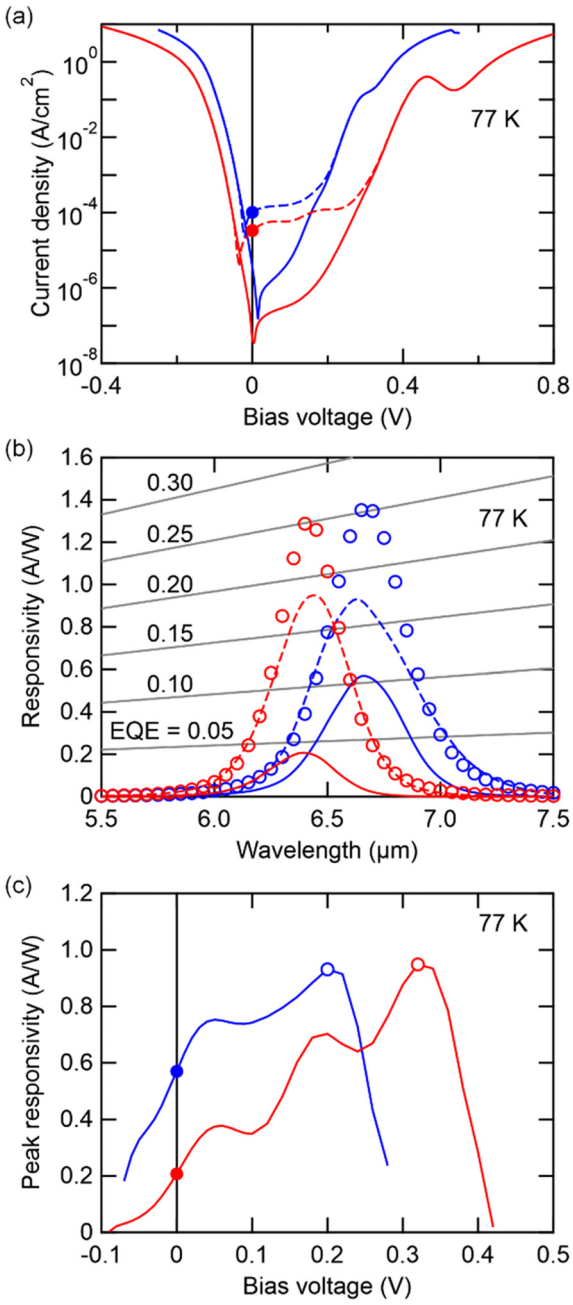

FIG. 4. (a) Current density–voltage relationship for QRD (red) and QCD (blue) for dark (solid) and background states (dotted) at 77 K. Filled circle: zero bias signal for 300-K background. (b) Responsivity spectra at 77 K for QRD and QCD. Solid lines: zero bias; dotted lines: peak bias (QRD: +0.32 V; QCD: +0.20 V); circles: calculation. Equiefficiency lines are also plotted. (c) Bias dependence of peak responsivity at 77 K. Filled circles: zero bias; open circles: peak bias.

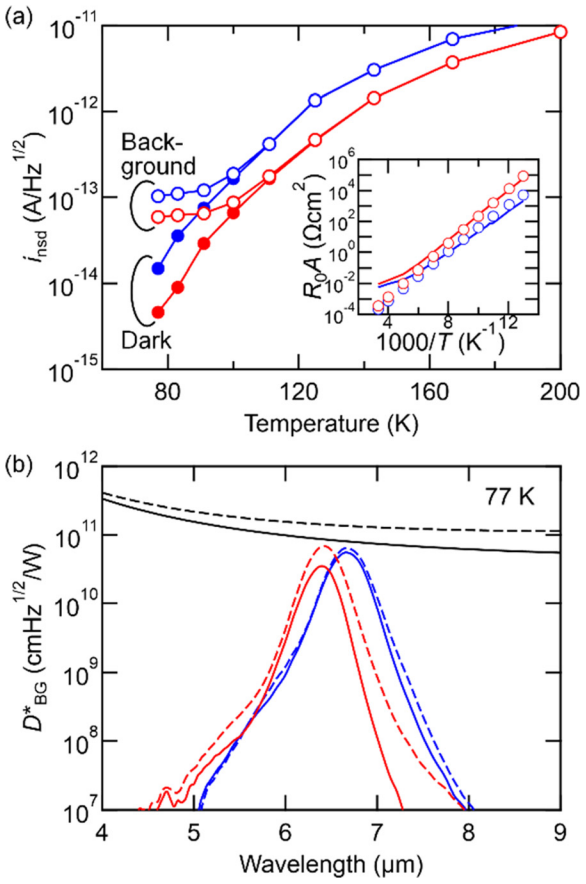

FIG. 5. (a) Temperature dependence of i_{nsd} for QRD (red) and QCD (blue). Filled circles: dark state; open circles: background state. Inset: temperature dependence of R_0A (line: experiment, circle: calculation). (b) D^*_{BG} spectra at 77 K for QRD (red) and QCD (blue). Solid lines: zero bias; dotted lines: peak bias. Black curves: theoretical limits. Solid line: interband detectors; dotted line: narrow-band detectors.

Both detectors present linear behavior throughout the temperature range studied and demonstrate fair agreement with the calculated values. The experimental activation energies derived from the slopes are 158 and 131 meV for QRD and QCD, respectively. In the band diagrams in Fig. 2, these activation energies with respect to Fermi energy are located between S_7 and S_6 for QRD and between S_6 and S_5 for QCD. This means that even S_5 influences the R_0A in the reference QCD. In contrast, S_6 of the QRD exerts a minor influence on R_0A, directly showing the advantage of the ratchet architecture.

Moreover, the observed $i_{nsd,DK}$'s are well described as $\sim(4k_BT/R_0)^{1/2}$ and thus surely limited by the Johnson noise. On the other hand, $i_{nsd,BG}$'s are constant below ~100 K for both detectors; i.e., both detectors are in the BLIP region. T_{BLIP}, defined as the temperature giving identical dark- and background-origin noise components ($2 \times i_{nsd,DK}{}^2 = i_{nsd,BG}{}^2$), is 98 and 94 K for QRD and QCD, respectively. All of these noise properties indicate the excellent performance of QRD.

Figure 5(b) shows the D^*_{BG} spectra at 77 K. At zero bias, D^*_{BG} values are 3.5×10^{10} and 5.5×10^{10} cmHz$^{1/2}$/W for QRD and QCD, respectively. As Eq. (4b) predicts, the QRD could not surpass the QCD with a higher R_{esp}. Nevertheless, a high R_0A makes possible a higher D^*_{BG} in a wider V_b range. Therefore, the maximum D^*_{BG} at a finite V_b again showed the higher performance of QRD: 6.8×10^{10} and 6.4×10^{10} cmHz$^{1/2}$/W for QRD ($V_b = +0.18$ V) and QCD

($V_b = +0.04$ V), respectively. If the R_{esp} of the QRD was raised by a factor of ~3 by improving the band alignment, zero bias D^*_{BG} equivalent to that of the QCD and a much higher D^*_{BG} at an optimum V_b could be achieved. In addition, T_{BLIP} as high as 110 K would be expected (see supplementary material S1 and S5).

Figure 5(b) also displays the theoretical limit of D^*_{BG} by black curves. The solid line corresponds to interband detectors; our detectors nearly meet this criterion. However, for narrow-band detectors like QWIPs, this limit does not apply.[15,35] The theoretical limit for a detector with a similar bandwidth (Gaussian profile with a full width at half maximum of 6%) is also plotted by the dotted line, showing that there is still room for improvement.

Finally, we comment on the temperature dependence of the responsivity. Many QCDs have demonstrated room-temperature responsivity, including the same material system as ours.[18] Nevertheless, both detectors in this study exhibited a quick responsivity drop at around $T = 140$ K, and we could not observe a significant signal at room temperature (see supplementary material S2 and S5). Because η_{abs} has no remarkable temperature dependence, the problem clearly lies elsewhere. Moreover, because this feature is common for both detectors, the problem is not due to the ratchet configuration. Our preliminary electron transport calculation suggests that the electron supply through our thick first barriers are bottlenecks at high temperatures. However, we would like to leave this for future work.

In summary, we proposed a PV-QWIP architecture with a drastically improved resistance by a step QW ratchetting the flow of electrons. Combined with optical antennas, a single-period detector demonstrated a maximum D^*_{BG} of 6.8×10^{10} cmHz$^{1/2}$/W at 6.4 μm, 77 K, and T_{BLIP} of 98 K for normal incidence. While severe requirement for band alignment was also revealed, these achievements would be sufficient for proving the significance of QRDs. Improvement of zero bias p_e by refining the design and fabrication is expected.

A step QW is a versatile structure with a large amount of design freedom, and it has demonstrated interesting opto-electronic functions. If a step QW were used as the active well, λ_p could be tuned by V_b,[36] although the spectral change in our QRD was not so substantial (see supplementary material S5). In particular, optical nonlinearity in step QWs has been extensively studied.[37] While a GaAs/AlGaAs material system is suitable for a wide mid-infrared range, this range can be further extended by antenna enhancement of nonlinearity, such as second harmonics. The QRD proposed here could serve as a starting point for fabricating diversified functional devices.

See the supplementary material for further details on theoretical calculations, fabrication, and characterization.

The authors are thankful for helpful discussions with a company choosing to remain anonymous, nextnano GmbH, M. F. Hainey, Jr., T. Ochiai, N. Ishida, Y. Sakuma, Y. Jimba, H. Miyazaki, K. Watanabe, H. Osato, A. Shigetou, Y. Arai, T. Kawazu, Y. Sugimoto, and A. Ohtake. This work was supported by JSPS KAKENHI Grant Nos. JP22K18990, JP23H01883, and JP24K01367 and by Advanced Research Infrastructure for Materials and Nanotechnology in Japan (ARIM) of the Ministry of Education, Culture, Sports, Science and Technology (MEXT), Proposal No. JPMXP1223 NM5062.

AUTHOR DECLARATIONS

Conflict of Interest

Yes, HTM has a Japanese patent (No. 2024–031328) pending.

Author Contributions

Hideki T. Miyazaki: Conceptualization (lead); Data curation (lead); Funding acquisition (lead); Investigation (equal); Methodology (lead); Software (lead); Validation (equal); Visualization (lead); Writing – original draft (lead). **Takaaki Mano:** Conceptualization (supporting); Data curation (supporting); Investigation (equal); Writing – review & editing (supporting). **Takeshi Noda:** Validation (equal); Writing – review & editing (lead). **Takeshi Kasaya:** Investigation (equal); Methodology (supporting); Software (supporting). **Yusuf B. Habibullah:** Investigation (equal).

DATA AVAILABILITY

The data that support the findings of this study are available from the corresponding author upon reasonable request.

REFERENCES

[1]Y. Yao, A. J. Hoffman, and C. F. Gmachl, Nat. Photonics **6**, 432–439 (2012).
[2]B. F. Levine, J. Appl. Phys. **74**, R1–R81 (1993).
[3]H. Schneider and H. C. Liu, *Quantum Well Infrared Photodetectors: Physics and Applications* (Springer, Berlin, 2007).
[4]W. A. Beck and M. S. Mirotznik, Infrared Phys. Technol. **42**, 189–198 (2001).
[5]W. Wu, A. Bonakdar, and H. Mohseni, Appl. Phys. Lett. **96**, 161107 (2010).
[6]Y. N. Chen, Y. Todorov, B. Askenazi, A. Vasanelli, G. Biasiol, R. Colombelli, and C. Sirtori, Appl. Phys. Lett. **104**, 031113 (2014).
[7]Q. Li, Z.-F. Li, N. Li, X.-S. Chen, P.-P. Chen, X.-C. Shen, and W. Lu, Sci. Rep. **4**, 6332 (2014).
[8]D. Palaferri, Y. Todorov, A. Bigioli, A. Mottaghizadeh, D. Gacemi, A. Calabrese, A. Vasanelli, L. Li, A. G. Davies, E. H. Linfield, F. Kapsalidis, M. Beck, J. Faist, and C. Sirtori, Nature **556**, 85–88 (2018).
[9]H. T. Miyazaki, T. Mano, T. Kasaya, H. Osato, K. Watanabe, Y. Sugimoto, T. Kawazu, Y. Arai, A. Shigetou, T. Ochiai, Y. Jimba, and H. Miyazaki, Nat. Commun. **11**, 565 (2020).
[10]C. Schönbein, H. Schneider, G. Bihlmann, K. Schwarz, and P. Koidl, Appl. Phys. Lett. **68**, 973–975 (1996).
[11]H. Schneider, C. Schönbein, M. Walther, K. Schwarz, J. Fleissner, and P. Koidl, Appl. Phys. Lett. **71**, 246–248 (1997).
[12]G. M. Penello, P. H. Pereira, M. P. Pires, D. Sivco, C. Gmachl, and P. L. Souza, Appl. Phys. Lett. **112**, 033503 (2018).
[13]D. Hofstetter, M. Beck, and J. Faist, Appl. Phys. Lett. **81**, 2683–2685 (2002).
[14]L. Gendron, M. Carras, A. Huynh, V. Ortiz, C. Koeniguer, and V. Berger, Appl. Phys. Lett. **85**, 2824–2826 (2004).
[15]F. R. Giorgetta, E. Baumann, M. Graf, Q. Yang, C. Manz, K. Kohler, H. E. Beere, D. A. Ritchie, E. Linfield, A. G. Davies, Y. Fedoryshyn, H. Jackel, M. Fischer, J. Faist, and D. Hofstetter, IEEE J. Quantum Electron. **45**, 1039–1052 (2009).
[16]A. Delga, "Quantum cascade detectors: A review," in *Mid-Infrared Optoelectronics* (Elsevier, 2020), pp. 337–377.
[17]S.-Q. Zhai, J.-Q. Liu, F.-Q. Liu, and Z.-G. Wang, Appl. Phys. Lett. **100**, 181104 (2012).
[18]A. Bigioli, G. Armaroli, A. Vasanelli, D. Gacemi, Y. Todorov, D. Palaferri, L. Li, A. G. Davies, E. H. Linfield, and C. Sirtori, Appl. Phys. Lett. **116**, 161101 (2020).
[19]Y. Zhu, S. Zhai, J. Liu, K. Li, K. Yang, S. Liu, J. Zhang, N. Zhuo, L. Wang, and F. Liu, Opt. Express **29**, 37327–37335 (2021).
[20]G. Quinchard, C. Mismer, M. Hakl, J. Pereira, Q. Lin, S. Lepillet, V. Trinité, A. Evirgen, E. Peytavit, J. L. Reverchon, J. F. Lampin, S. Barbieri, and A. Delga, Appl. Phys. Lett. **120**, 091108 (2022).

[21]T. Dougakiuchi, K. Fujita, T. Hirohata, A. Ito, M. Hitaka, and T. Edamura, Appl. Phys. Lett. **109**, 261107 (2016).
[22]B. Schwarz, P. Reininger, A. Harrer, D. MacFarland, H. Detz, A. M. Andrews, W. Schrenk, and G. Strasser, Appl. Phys. Lett. **111**, 061107 (2017).
[23]L. Gendron, C. Koeniguer, V. Berger, and X. Marcadet, Appl. Phys. Lett. **86**, 121116 (2005).
[24]A. Vardi, G. Bahir, F. Guillot, C. Bougerol, E. Monroy, S. E. Schacham, M. Tchernycheva, and F. H. Julien, Appl. Phys. Lett. **92**, 011112 (2008).
[25]P. Reininger, T. Zederbauer, B. Schwarz, H. Detz, D. MacFarland, A. M. Andrews, W. Schrenk, and G. Strasser, Appl. Phys. Lett. **107**, 081107 (2015).
[26]P. Reininger, B. Schwarz, H. Detz, D. MacFarland, T. Zederbauer, A. M. Andrews, W. Schrenk, O. Baumgartner, H. Kosina, and G. Strasser, Appl. Phys. Lett. **105**, 091108 (2014).
[27]E. Rosencher, P. Bois, J. Nagle, E. Costard, and S. Delaitre, Appl. Phys. Lett. **55**, 1597–1599 (1989).
[28]G. Leveque and O. J. F. Martin, Opt. Lett. **31**, 2750–2752 (2006).
[29]H. T. Miyazaki and Y. Kurokawa, Phys. Rev. Lett. **96**, 097401 (2006).
[30]J. L. Perchec, Y. Desieres, and R. Espiau de Lamaestre, Appl. Phys. Lett. **94**, 181104 (2009).
[31]C. Koeniguer, G. Dubois, A. Gomez, and V. Berger, Phys. Rev. B **74**, 235325 (2006).
[32]R. Ferreira and G. Bastard, Phys. Rev. B **40**, 1074–1086 (1989).
[33]T. Mano, H. T. Miyazaki, T. Kasaya, T. Noda, and Y. Sakuma, ACS Omega **4**, 7300–7307 (2019).
[34]M. F. Hainey, Jr., T. Mano, T. Kasaya, Y. Jimba, H. Miyazaki, T. Ochiai, H. Osato, K. Watanabe, Y. Sugimoto, T. Kawazu, Y. Arai, A. Shigetou, and H. T. Miyazaki, Opt. Express **29**, 59–69 (2021).
[35]M. F. Hainey, Jr., T. Mano, T. Kasaya, Y. Jimba, H. Miyazaki, T. Ochiai, H. Osato, Y. Sugimoto, T. Kawazu, A. Shigetou, and H. T. Miyazaki, Opt. Express **29**, 43598–43611 (2021).
[36]E. Martinet, F. Luc, E. Rosencher, P. Bois, and S. Delaitre, Appl. Phys. Lett. **60**, 895–897 (1992).
[37]E. Rosencher, A. Fiore, B. Vinter, V. Berger, P. Bois, and J. Nagle, Science **271**, 168–173 (1996).